J Inorg Organomet Polym (2014) 24:722–728
DOI 10.1007/s10904-014-0031-2

$SrFe_{12}O_{19}/Zn_{0.65}Ni_{0.25}Cu_{0.1}Fe_2O_4$ Core–Shell Nanocomposite: Synthesis, Chracterization and Catalytic Activity in Aqueous Solution

S. Esir · Y. Junejo · A. Baykal · M. Toprak · H. Sözeri

Received: 24 December 2013 / Accepted: 28 March 2014 / Published online: 12 April 2014

Abstract $SrFe_{12}O_{19}/Zn_{0.65}Ni_{0.25}Cu_{0.1}Fe_2O_4$ core–shell nanocomposite has been successfully synthesized by sol–gel autocombustion (for $SrFe_{12}O_{19}$, core) and hydrothermal methods (for $Zn_{0.65}Ni_{0.25}Cu_{0.1}Fe_2O_4$, shell). The products were characterized by X-ray powder diffractometer, transmission electron microscopy, fourier transform infrared spectrsocopy, vibrating sample magnetometer, Ultraviolet–visible specroscopy and inductively coupled plasma. Both X-ray powder diffraction, transmission electron microscopy results showed that $Zn_{0.65}Ni_{0.25}Cu_{0.1}Fe_2O_4$ shell is on the surface of the $SrFe_{12}O_{19}$ core. The variations between the magnetic properties of the precursors and nanocomposite may be explained by interphase interactions at the surface of two ferrites. The properties of the $SrFe_{12}O_{19}/Zn_{0.65}Ni_{0.25}Cu_{0.1}Fe_2O_4$ core–shell nanocomposite were favourable in its separation, recycling and reuse after reaction. The catalytic activity of $SrFe_{12}O_{19}/Zn_{0.65}Ni_{0.25}Cu_{0.1}Fe_2O_4$ core–shell nanocomposite in the presence of $NaBH_4$ were tested against methyl violet.

Keywords Magnetic materials · Chemical synthesis · X-ray diffraction · Catalytic properties · Magnetic properties · Methyl violet

1 Introduction

Synthetic dyes, which are widely used in many industrial processes (textile, paper printing and photography), can absorb and reflect sunlight and, therefore, can intefere with the growth of bacteria and stop photosynthesis in aquatic environments. Depending on the exposure time and dye concentration, they have a chronic effect on organisms [1–3]. Due to the mutagenic and carcinogenic effects, the removal of these dyes from waste-water is of great interest.

As compared to azo dyes, methyl violet (MV, triphenyl methane dye), which is used mostly in gram-staining and as an antiallergenic acid, is difficult to degrade. It can also be used as a moderate-class disinfectant; however, it is very poisonous most animals. Inhalation of MV may also cause irritation of the respiratory tract, whereas ingestion causes irritation to the gastrointestinal tract. When living organisms (animals and humans) come in contact with MV, it causes pain and congestion [4–6].

The combination of hexaferrites (high saturation magnetization and large anisotropy field) and spinel ferrites (strong anisotropy, high coercivity and moderate saturation magnetization at room temperature) can improve the magnetic and electromagnetic absorption properties of ferrite materials.

The main prupose of much research related to hexaferrite–spinel compounds is based on merging the high

S. Esir (✉) · Y. Junejo · A. Baykal
Department of Chemistry, Fatih University, 34500 B.Çekmece, Istanbul, Turkey
e-mail: snmesir@gmail.com

Y. Junejo
National Center of Excellence in Analytical Chemistry, University of Sindh Jamshoro, Jamshoro 76080, Pakistan

M. Toprak
Department of Materials Science and Engineering, Yildirim Beyazit University, Ulus, Ankara, Turkey

M. Toprak
Department of Materials and Nano Physics, KTH-Royal Institute of Technology, 16440 Stockholm, Sweden

H. Sözeri
TUBITAK-UME, National Metrology Institute, P.O. Box 54, 41470 Gebze, Kocaeli, Turkey

anisotropy of hard magnet compounds with large magnetization of the soft magnetic materials, which improve their magnetic and elecromagetic absorption properties of materials [7–11]. Theoretical studies reveal that the magnetic properties of nanocomposite permanent magnets are strongly dependent on the grain size of the hard and soft phases as well as the nature of magnetic interactions between them [12, 13].

There are many studies related with the use of magnetically recycable catalysts for various organic reactions. Baig et al. [14] reported a magnetic silica-supported ruthenium catalyst for the hydrogenetion of carbonyl compounds. Pourjavadi et al. [15] used a magnetic recoverable catalyst as a green catalyst for the protection of aldehydes by a solvent-free conversion to 1,1-diacetate at room temperature. An et al. [16] synthesized a nanocomposite catalyst containing both magnetite (Fe_3O_4) and palladium nanoparticles with magnetic separation and recyclability for the catalytic hydrogenation of 4-nitrophenol. In another study, Ma et al. [17] synthesized multifunctional inorganic–organic hybrid nanospheres for rapid and selective luminescence detection of TNT in mixed nitroaromatics via magnetic separation.

The aim of this paper is to develop magnetic recyclable nanocomposite catalysts based on a $SrFe_{12}O_{19}/Zn_{0.65}Ni_{0.25}Cu_{0.1}Fe_2O_4$ core–shell nanocomposite using a combination of sol–gel autocombustion (for SrM) and hydrothermal (for $Zn_{0.65}Ni_{0.25}Cu_{0.1}Fe_2O_4$ NPs) methods, followed by the investigation of their catalytic effect on the degradation of the MV dye.

2 Experimental

2.1 Chemicals and Instrumentation

Strontium chloride dihydrate ($SrCl_2{\cdot}2H_2O$; 98 %), iron (III) nitrate nonahydrate [$Fe(NO_3).9H_2O$; 98 %], $Zn(NO_3)_2{\cdot}6H_2O$, $Ni(NO_3)_2{\cdot}6H_2O$, $Cu(NO_3)_2{\cdot}3H_2O$, ethanol, $NaBH_4$, and NaOH were obtained from Merck and were used as received without further purification.

X-ray powder diffraction (XRD) analysis was conducted with a Rigaku Smart Lab Diffractometer operated at 40 kV and 35 mA using Cu K_α radiation.

High resolution transmission electron microscopy (HR-TEM) analysis was performed using a JEOL JEM 2100 microscope. A drop of diluted sample in alcohol was dripped on a TEM grid.

Fourier transform infrared (FT-IR) spectra were recorded in transmission mode (Perkin Elmer BX FT-IR) on powder samples that were ground with KBr and compressed into a pellet. FT-IR spectra from 4,000 to 400 cm^{-1} were recorded in order to investigate the nature of the chemical bonds formed.

VSM measurements were performed by using a Vibrating sample magnetometer (LDJ Electronics Inc., Model 9600). The magnetization measurements were carried out in an external field up to 15 kOe at room temperature.

inductively coupled plasma-OES analysis was performed by using the Perkin Elmer Optima 4300DV model.

UV–vis measurements were performed using a Shimadzu UV–Vis 2600. Catalytic efficiency of degradation of the MV dye was assesed using UV–Vis spectroscopy, focusing on the typical absorption of MV at 585 nm..

2.2 Procedure

2.2.1 *Synthesis of $SrFe_{12}O_{19}$ NPs*

For the synthesis of $SrFe_{12}O_{19}$ NPs, citrate sol–gel combustion method was applied. Stoichiometric amounts of $Sr(NO_3)_2{\cdot}2H_2O$ and $Fe(NO_3){\cdot}9H_2O$ were dissolved in deionized water to achive a Fe/Sr molar ratio of 8. Then, mixed aqueous solution was heated for 1 h at 80 °C under vigorous stirring. A specific amount of citric acid was then added to this mixture (molar ratio of citric acid to metal ions used were 1:1). Ammonia was added to adjust the pH value to 7. The clear solution was slowly evaporated at 80 °C under constant stirring, forming a viscous gel. By increasing the temperature up to 200 °C, the gel precursors were combusted to form black powders. Finally, the obtained powder was calcined at 450 °C for 4 h and at 1,100 °C for 1 h.

2.2.2 *Synthesis of $SrFe_{12}O_{19}$ (hard)/$Zn_{0.65}Ni_{0.25}Cu_{0.1}Fe_2O_4$ Core–Shell Nanocomposite with Hydrothermal Method*

The appropriate amount of nitrates [$Fe(NO_3).9H_2O$, $Zn(NO_3)_2{\cdot}6H_2O$, $Ni(NO_3)_2.6H_2O$, and $Cu(NO_3)_2.3H_2O$] were dissolved in deionized water. Mixed aqueous solution was heated for 1 h at 80 °C under vigorous stirring. Citric acid was then added to this mixture, maintaining a molar ratio of citric acid to metal ions of 1:1. Ammonia was used to adjust the pH value to 11. Then, 0.125 g of synthesized $SrFe_{12}O_{19}$ NPs were added to this mixture. Finally this solution was transferred into a Teflon-lined stainless steel autoclave and was heated at 250 °C for 24 h. After treatment, the autoclave was allowed to cool down and the precipitates were collected, centrifuged for 10 min and supernatant was discarded. The obtained particles were washed three times with ethanol and distilled water in order to remove impurities, and then dried at 80 °C overnight.

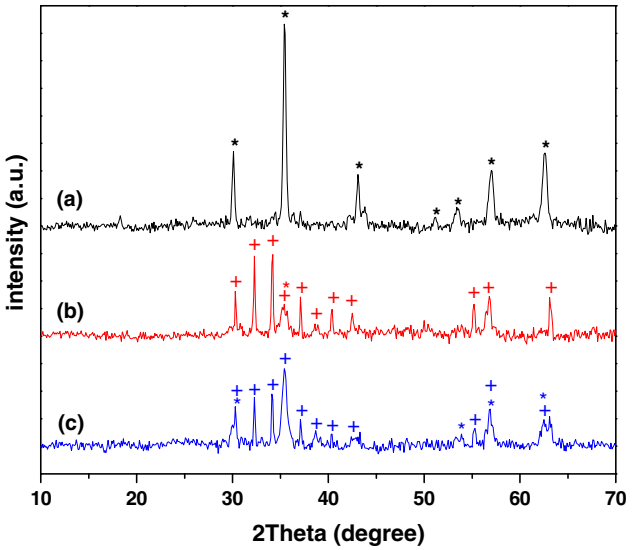

Fig. 1 XRD powder patterns of *a* $Zn_{0.65}Ni_{0.25}Cu_{0.1}Fe_2O_4$ NPs, *b* $SrFe_{12}O_{19}$ NPs and *c* $SrFe_{12}O_{19}/Zn_{0.65}Ni_{0.25}Cu_{0.1}Fe_2O_4$ core–shell nanocomposite (Color figure online)

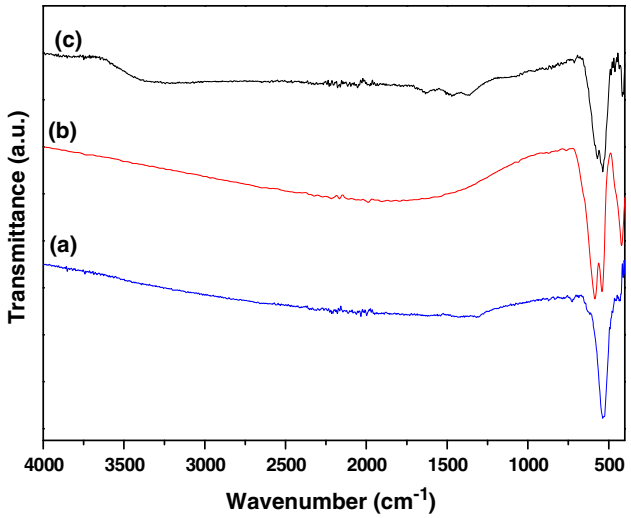

Fig. 2 FT-IR spectra of *a* $Zn_{0.65}Ni_{0.25}Cu_{0.1}Fe_2O_4$, *b* $SrFe_{12}O_{19}$, and *c* $SrFe_{12}O_{19}/Zn_{0.65}Ni_{0.25}Cu_{0.1}Fe_2O_4$ core–shell nanocomposite (Color figure online)

3 Results and Discussion

3.1 XRD Analysis

Figure 1a–c show the XRD patterns of the prepared $SrFe_{12}O_{19}$ NPs, $Zn_{0.65}Ni_{0.25}Cu_{0.1}Fe_2O_4$ NPs and $SrFe_{12}O_{19}/Zn_{0.65}Ni_{0.25}Cu_{0.1}Fe_2O_4$ core–shell nanocomposite, respectively (to show the existence of $Zn_{0.65}Ni_{0.25}Cu_{0.1}Fe_2O_4$ and $SrFe_{12}O_{19}$ NPs in the product, $Zn_{0.65}Ni_{0.25}Cu_{0.1}Fe_2O_4$ NPs and $SrFe_{12}O_{19}$ NPs were synthesized separately according to the given procedure above). All the diffraction peaks are in good agreement with the cubic phase of $Zn_{0.65}Ni_{0.25}Cu_{0.1}Fe_2O_4$ (Fig. 1a) and hexagonal structure of $SrFe_{12}O_{19}$ (Fig. 1b); the peaks are broadened due to their nanometric crystallite sizes. The average crystallite size of $SrFe_{12}O_{19}$ and $Zn_{0.65}Ni_{0.25}Cu_{0.1}Fe_2O_4$ concluded from the Scherrer equation is about 16 and 25 nm, respectively. The XRD pattern of $SrFe_{12}O_{19}/Zn_{0.65}Ni_{0.25}Cu_{0.1}Fe_2O_4$ nanocomposite, shown in Fig. 1c, displays XRD peaks of both $SrFe_{12}O_{19}$ and $Zn_{0.65}Ni_{0.25}Cu_{0.1}Fe_2O_4$, revealing the co-existence of hexaferrite and spinel ferrite phases in the nanocomposite [18–21].

3.2 FT-IR Analysis

Figure 2 showed the FT-IR spectra of $Zn_{0.65}Ni_{0.25}Cu_{0.1}Fe_2O_4$, $SrFe_{12}O_{19}$ NPs and $SrFe_{12}O_{19}/Zn_{0.65}Ni_{0.25}Cu_{0.1}Fe_2O_4$ core–shell nanocomposite. The band representing the metal–oxygen bonds occurs at $\sim$550 cm^{-1}; this is the characteristic absorption peak of the spinel structure (Fig. 2a). The characteristic peaks of hexaferrite (Fig. 2b) are observed at 605 and 555 cm^{-1}, and at $\sim$450 cm^{-1} [18–22]. The FT-IR spectra of the $SrFe_{12}O_{19}/Zn_{0.65}Ni_{0.25}Cu_{0.1}Fe_2O_4$ nanocomposite has both of these vibration peaks (Fig. 2c).

The spectrum for the solution after the degradation process reveals typical bands; at $\sim$1,650 and 3,300 cm^{-1}. The first band is ascribed to C=O and the second to N–H bond [23]. The observed spectrum is similar to that of tertiary amines [23]. Therefore, it is proposed that the degradation product is most likely a tertiary amine. Based on this observation, it is suggested that the aromatic rings cleaves and fragment to form alkyl groups, which tether to nitrogen to form a tertiary amine.

3.3 ICP Analysis

A small amount of powder was dissolved in acid and used for the detemrination of the concentration of metal ions in order to determine the composition of ferrites and the ratio of hexaferrite to ferrite. The weight percentages of Sr, Fe, Zn, Cu, and Ni are 5.9, 58.3, 5.2, 4.9, 4.4, respectively. Based on these results, the ratio of hexaferrite to ferrite $SrFe_{12}O_{19}/Zn_{0.65}Ni_{0.25}Cu_{0.1}Fe_2O_4$ is 1:1.

3.4 TEM Analysis

The morphology of he synthesized $SrFe_{12}O_{19}/Zn_{0.65}Ni_{0.25}Cu_{0.1}Fe_2O_4$ core–shell nanocomposite was investigated by TEM. Several micrographs are shown in Fig. 3. The particles are clustered to 100–200 nm size aggregates.

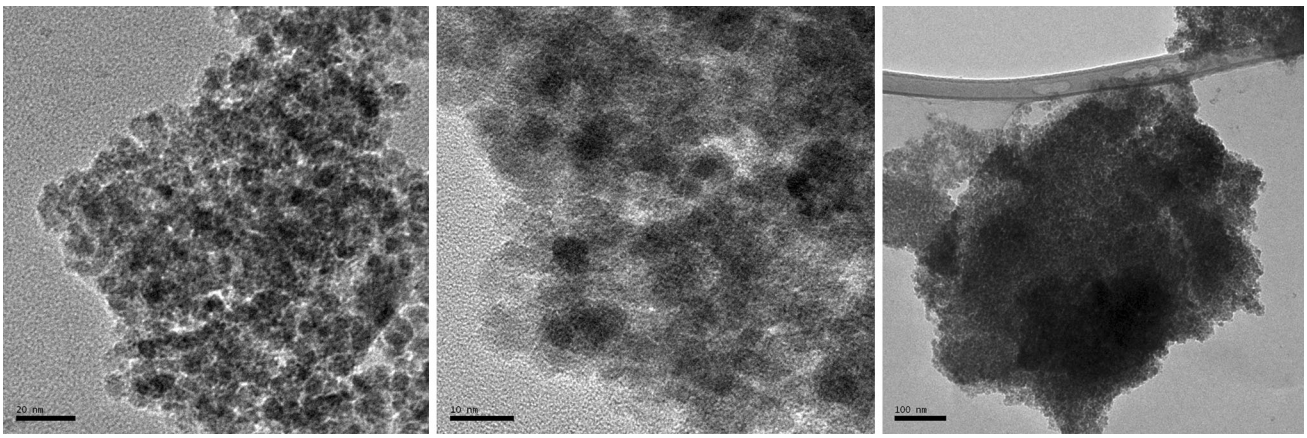

Fig. 3 TEM micrographs of $SrFe_{12}O_{19}/Zn_{0.65}Ni_{0.25}Cu_{0.1}Fe_2O_4$ core–shell nanocomposite with different magnifications

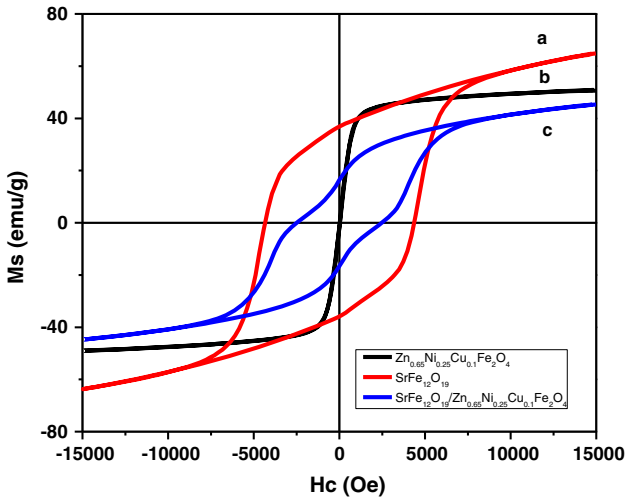

Fig. 4 M–H hysterisis curves of *a* $SrFe_{12}O_{19}$ NPs, *b* $Zn_{0.65}Ni_{0.25}Cu_{0.1}Fe_2O_4$ NPs, *c* $SrFe_{12}O_{19}/Zn_{0.65}Ni_{0.25}Cu_{0.1}Fe_2O_4$ core–shell nanocomposite (Color figure online)

The different contrast in the TEM may be attributed to dark hexaferrite ($SrFe_{12}O_{19}$) and bright ferrite ($Zn_{0.65}Ni_{0.25}Cu_{0.1}Fe_2O_4$) compositions of the nanoparticles. The TEM images reveal that the $SrFe_{12}O_{19}/Zn_{0.65}Ni_{0.25}Cu_{0.1}Fe_2O_4$ nanocomposite has a core–shell structure. $Zn_{0.65}Ni_{0.25}Cu_{0.1}Fe_2O_4$ shells are formed on the surface of the $SrFe_{12}O_{19}$ NPs. Due to the hard magnetic properties of the hexaferrites, $SrFe_{12}O_{19}$ NPs absorb more electrons than the $Zn_{0.65}Ni_{0.25}Cu_{0.1}Fe_2O_4$ spinel structure. The particle size of the dark ($SrFe_{12}O_{19}$) and bright ($Zn_{0.65}Ni_{0.25}Cu_{0.1}Fe_2O_4$) region in the TEM images are consistent with the crystallite size obtained from the XRD powder patterns.

3.5 VSM Analysis

Magnetic characterization of the $SrFe_{12}O_{19}/Zn_{0.65}Ni_{0.25}Cu_{0.1}Fe_2O_4$ core–shell nanocomposite is shown in Fig. 4. Clearly, the M–H hysterisis curves of both samples do not have a single phase behaviour. There appears to be a superposition of two loops corresponding to the soft and hard ferrites. This also means that there is no exchange coupling between the hard $SrFe_{12}O_{19}$ core and soft $Zn_{0.65}Ni_{0.25}Cu_{0.1}Fe_2O_4$ shell. According to the theoretical calculations, exchange coupling is more probable only if the dimension of the soft phase is smaller than a critical length, which is typically twice or less than the domain wall width of the hard phase [10, 24–27]. The domain wall width of the $SrFe_{12}O_{19}$ hard ferrite is approximately 9 nm [28]. Therefore, if the thickness of the $Zn_{0.65}Ni_{0.25}Cu_{0.1}Fe_2O_4$ is larger than 18 nm or less than 9 nm, coupling does not occur, which is probably the case for the nanocomposites in this study.

In two-phase magnetic materials, there are two main interactions; exchange and dipolar, that determine the magnetic property of the material. Moreover, there are three exchange energy terms that need to be taken into account; i.e., exchange energy between the soft and the hard (which is dominating), between soft and soft and between hard and hard phases. If dipolar interaction is neglected, magnetization in the remanence state is mainly determined by the exchange interaction and magnetocrystalline anisotropy. If the concentration of the soft magnetic phase is greater than some threshold, exchange interaction cannot suppress the dipolar interaction and, thus, a magnetic vortex state appears in the center of the soft regions [10]. As a result, one would observe a "kink" in the M–H hysterisis loops. We can also state that if the concentration of the soft phase is a slightly less than its present value in the coprecipitated sample, an observe exchange spring behavior due to weakness of the dipolar interaction would be observed. The magnetic parameters of the two core–shell NPs wearere given in Table 1. Clearly, the value of the saturation magnetization Ms decreases from ~65 emu/g

Table 1 Magnetic parameters of the $SrFe_{12}O_{19}/Zn_{0.65}Ni_{0.25}Cu_{0.1}Fe_2O_4$ core–shell nanocomposite

	Ms (emu/g)	H_c (Oe)
$SrFe_{12}O_{19}$	65	4,480
$Zn_{0.65}Ni_{0.25}Cu_{0.1}Fe_2O_4$	51	50
$SrFe_{12}O_{19}/Zn_{0.65}Ni_{0.25}Cu_{0.1}Fe_2O_4$	45	2,400

for $SrFe_{12}O_{19}$ to ~45 emu/g for the core–shell structure nanocomposites owing to the coating of $Zn_{0.65}Ni_{0.25}Cu_{0.1}Fe_2O_4$ NPs (Table 1). And, the coercivity Hc of $SrFe_{12}O_{19}/Zn_{0.65}Ni_{0.25}Cu_{0.1}Fe_2O_4$ core–shell nanocomposite (2,400 Oe) is intermediate between that of $SrFe_{12}O_{19}$ (4,480 Oe) and $Zn_{0.65}Ni_{0.25}Cu_{0.1}Fe_2O_4$ (70 Oe). The change in the saturation magnetization and coercivity may be attributed to the existence of $Zn_{0.65}Ni_{0.25}Cu_{0.1}Fe_2O_4$ on the surface of the $SrFe_{12}O_{19}$ NPs, which can result in interparticle interaction at the interface of the two phases [29]. This decrease in Ms in core–shell structure may be related to the

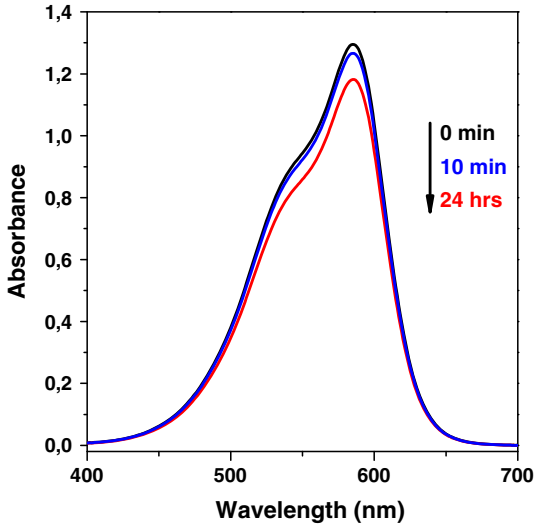

Fig. 5 UV–visible spectra for the degradation of MV in aqueous solution in the presence of $NaBH_4$ (Color figure online)

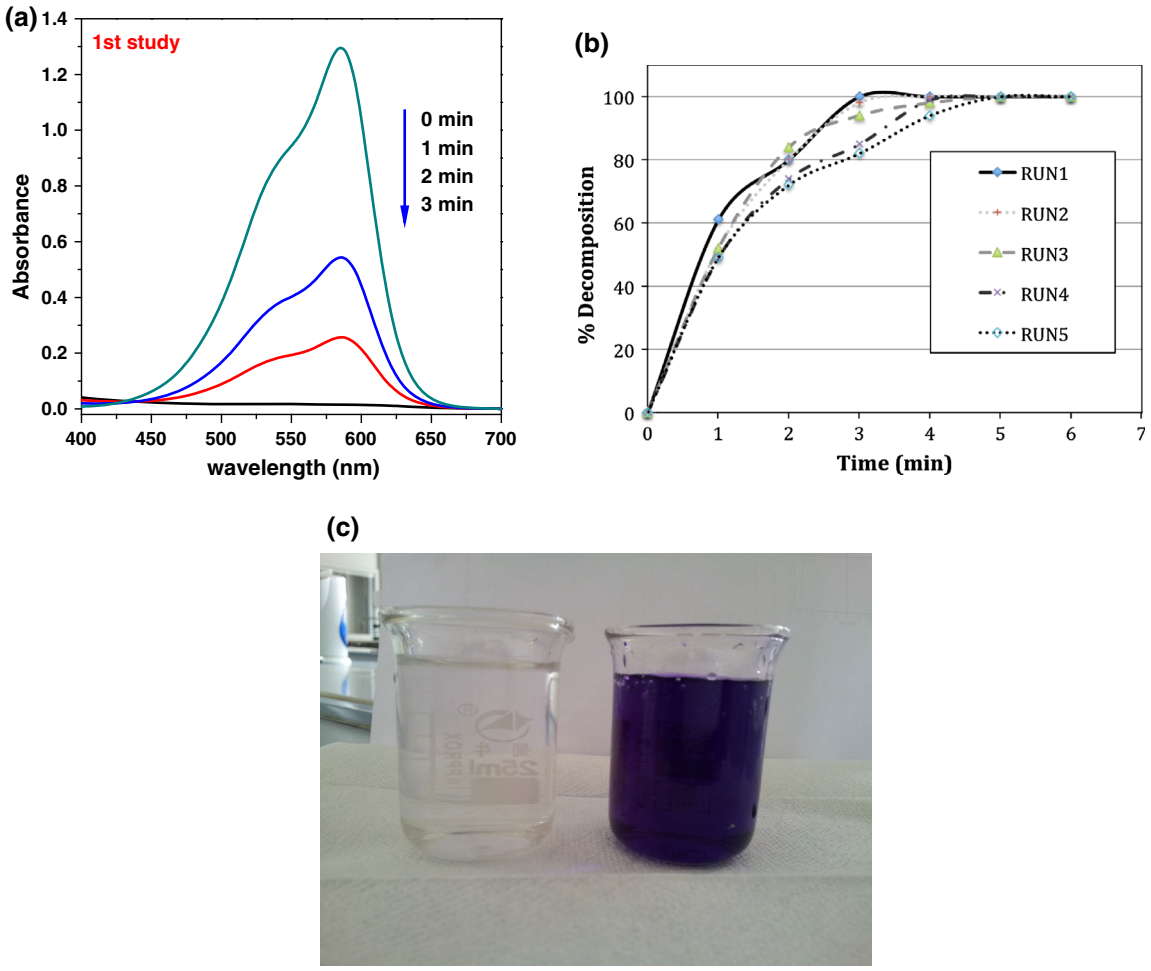

Fig. 6 **a** UV–visible spectra for degradation of MV in aqueous solution containing $SrFe_{12}O_{19}/Zn_{0.65}Ni_{0.25}Cu_{0.1}Fe_2O_4$ core–shell nanocomposite, **b** for subsequent five runs, **c** color of MV is *violet* but after catalysis it turned as *colorless* (Color figure online)

adsorption of $Zn_{0.65}Ni_{0.25}Cu_{0.1}Fe_2O_4$ NPs to the surface of SrM through oxygen atoms. It is well know that magnetization of hexaferrites is strongly related to the strength of Fe–O-Fe exchange interaction. If some of the oxide ions on the NP surface are used during the adsorption, then exchange interaction weakens. As a result, magnetization of the core–shell NPs may be less than that of the pure Sr-hexaferrite.

3.6 Degradation Study

3.6.1 UV–Vis Analysis

MV is originally violet and turns colorless on degradation. This makes it easy to follow the process by UV–Vis analysis. A 10 μM solution of MV is added to 0.1 ml of 0.1 M $NaBH_4$. The UV–Vis spectra of the mixture is recorded as a function of time (Fig. 5). A very small degree of degradation is observed by the addition of the reducing agent $NaBH_4$ as assessed by the absorption intensity at 580 nm,. When the same experiment is repeated on addition of 0.1 mg of ferrite/hexaferrite nanocomposite powder, a large reduction of absorption intensity is observed within minutes (Fig. 6). This demonstrates the catalytic efficiency of the nanocomposite, which reveals a large decay in MV concentration in the presence of the nanocomposite (Fig. 6a). The peak at 585 nm decreases gradually by the addition of nanoparticles and disappears completely within 3 min. When the same experiment is carried out in the absence of the nanocomposite and presence of reducing agent, only a very small reduction is observed over 24 h. Thus, these nanoparticles are found to be highly dynamic catalysts for the mentioned reduction processes. Pal et al. [30] reported the degradation of MV using platinium nanoparticles synthesized by the microwave assisted method. They reduced MV by photodegradation in 20 min. In our study, the degradation is rapid (within 3 min). The other advantage is the ease of recovery and re-use of the magnetic nanocomposite [31, 32]. The color of MV before catalysis is violet; after catalysis MV turns colorless (Fig. 6c).

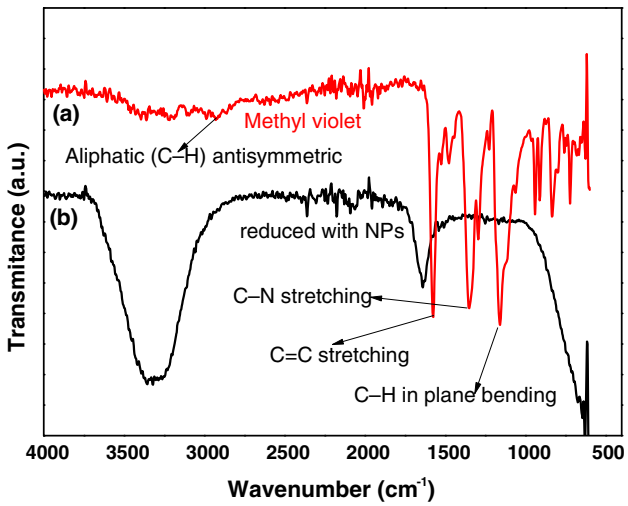

Fig. 7 FT-IR spectra of MV *a* before and *b* after catalysis with $SrFe_{12}O_{19}/Zn_{0.65}Ni_{0.25}Cu_{0.1}Fe_2O_4$ core–shell nanocomposite (Color figure online)

3.6.2 FT-IR Analysis

Catalytic degradation of MV was monitored with FT-IR spectroscopy. Characteristic FT-IR peaks for MV are seen in Fig. 7. After catalysis in the presence of the $SrFe_{12}O_{19}/Zn_{0.65}Ni_{0.25}Cu_{0.1}Fe_2O_4$ nanocomposite, all the functional peaks of MV disappear [33].

4 Conclusion

A $SrFe_{12}O_{19}/Zn_{0.65}Ni_{0.25}Cu_{0.1}Fe_2O_4$ core–shell nanocomposite was prepared by a combination of sol–gel auto-combustion and hydrothermal methods. XRD patterns revealed the co-presence of $SrFe_{12}O_{19}$ (hexaferrite) and $Zn_{0.65}Ni_{0.25}Cu_{0.1}Fe_2O_4$ (spinel ferrite) nanoparticles. The results of VSM indicate that the saturation magnetization and coercivity of the nanocomposite are less than the core material $SrFe_{12}O_{19}$. The saturation magnetization and the coercivity decrease from 65.4 emu/g for $SrFe_{12}O_{19}$ to 45.4 emu/g for $SrFe_{12}O_{19}/Zn_{0.65}Ni_{0.25}Cu_{0.1}Fe_2O_4$ nanocomposite. The nanocomposite shows strong reducing character, which is demonstrated by the degradation within minutes of a model dye (MV) molcule. A novel characteristic of the material is achieved by the combination of spinel ferrites and hexaferrites. The mechanism is still under investigation.

References

1. D.A. Oxspring, G. McMullan, W.F. Smyth, R. Marchant, Biotechnol. Lett. **18**, 527 (1996)
2. I.M. Robinson, G. McMillan, R. Marchant, P. Nigam, Bioresour. Technol. **77**, 247 (2001)
3. Y.M. Slokar, A.M. Le Marechal, Dyes Pigm. **37**, 335 (1998)
4. Y.L. Liu, Y.F. Du, J.X. Lu, Chin. Shanghai Environ. Sci. **22**, 888 (2003)
5. A. Mittal, V. Gajbe, J. Mittal, J. Hazard. Mater. **150**, 364 (2008)
6. Y. Tiana, C. Jia, M. Zhao, M. Xu, Y. Zhang, R. Wang, Chem. Eng. J. **165**, 474 (2010)
7. M.H. Yu, J.H. Hatrick-Simpers, I. Takeuchi, J. Li, Z.L. Wang, J.P. Liu, S.E. Lofland, S. Tyagi, J.W. Freeland, D. Giubertoni, M. Bersani, M. Anderli, J. Appl. Phys. **8**, 1 (2005)
8. Z.J. Guo, J.S. Jiang, J.E. Pearson, S.D. Bader, J.P. Liu, Appl. Phys. Lett. **81**, 2029 (2002)

9. L. Zhang, Z. Li, J. Alloys Compd. **469**, 422 (2009)
10. D. Roy, C. Shivakumara, P.S. Anil, kumar. J. Magn. Magn. Mater. **321**, L11 (2009)
11. M.A. Radmanesh, S.A. Seyyed, Ebrahimi. J. Magn. Magn. Mater. **324**, 3094 (2012)
12. J.S. Jiang, J.E. Pearson, Z.Y. Liu, B. Kabius, S. Trasobares, D.J. Miller, S.D. Bader, D.R. Lee, D. Haskel, G. Srajer, J.P. Liu, Appl. Phys. Lett. **85**, 5293 (2004)
13. D. Wu, Q. Zhang, J. Ping Liu, R.F. Sabirianov, J. Nanoscale Sci. Technol. **8**, 3036 (2008)
14. R.B.N. Baig, R.S. Varma, ACS Sustain. Chem. Eng. **1**, 805 (2013)
15. A. Pourjavadi, S.H. Hossein, M. Doulabi, S.M. Fakoorpoor, F. Seidi, ACS **2**, 1259 (2012)
16. M. An, J. Cui, L. Wang, J. Phys. Chem. C **118**, 3062 (2014)
17. Y. Ma, S. Huang, L. Wang, Talanta **116**, 535 (2013)
18. A. Baykal, M.S. Toprak, Z. Durmus, H. Sozeri, J. Supercond. Nov. Magn. **25**, 2081 (2012)
19. Y. Köseoğlu, A. Baykal, M.S. Toprak, F. Gözüak, A.C. Başaran, B. Aktaş, J. Alloys Compd. **462**, 209 (2008)
20. T.G. Altincekic, İ. Boz, A. Baykal, S. Kazan, R. Topkaya, M.S. Toprak, J. Alloys Compd. **493**, 493 (2010)
21. M. Demirelli, E. Karaoğlu, A. Baykal, H. Sözeri, E. Uysal, O. Duygulu, J. Inorg. Organomet. Polym Mater. **23**, 937 (2013)
22. T. Xie, L. Xu, C. Liu, Y. Wang, Appl. Surf. Sci. **273**, 684 (2013)
23. http://www.sigmaaldrich.com/catalog/product/fluka/86891
24. E.F. Kneller, R. Hawig, IEEE Trans. Magn. **27**, 3588 (1993)
25. R. Skomski, J.M.D. Coey, Phys. Rev. B **48**, 15812–15816 (1993)
26. T. Schrefl, H. Kronmiiller, J. Fidler, J. Magn. Magn. Mater. **127**, L273 (1993)
27. Z.S. Shan, J.P. Liu, V.M. Chakka, H. Zeng, J.S. Jiang, IEEE Trans. Magn. **38**, 2907 (2002)
28. P.E. Garcia-Casillas, A.M. Beesley, D. Buenoc, J.A. Matutes-Aquino, C.A. Martinez, J. Alloys Compd. **369**, 185 (2004)
29. N. Chen, G.H. Mu, X.F. Pan, K.K. Gan, M.Y. Gu, Mater. Sci. Eng., B **139**, 256 (2007)
30. J. Pal, M.K. Deb, D.K. Deshmukh, B.K. Sen. Microwave-assisted synthesis of platinum nanoparticles and their catalytic degradation of methyl violet in aqueous solution. Appl. Nanosci. doi:10.1007/s13204-012-0170-0
31. L. Zhou, J. Huang, B. He, F. Zhang, H. Li, Carbohydr. Polym. **101**, 574 (2014)
32. B. Karthikeyann, L. Natanapatham, S. Senthilvelan, V.L. Chandraboss, M. Murugavelu, Mater. Sci. Semicond. Process. **16**, 23 (2013)
33. H.M. Zeyada, M.M. EL-Nahass, I.S. Elashmawi, A.A. Habashi, J. Non-Cryst. Solids **358**, 625 (2012)